An Equivariant Graph Network for Interpretable Nanoporous Materials Design

Zhenhao Zhou[1,2], Salman Bin Kashif[3], Dawei Feng[4], Jin-Hu Dou[5], Kaihang Shi[3]*, Tao Deng[1], Zhenpeng Yao[1,2]*

[1]Center of Hydrogen Science and School of Materials Science and Engineering, Shanghai Jiao Tong University, Shanghai 200240, China

[2]Innovation Center for Future Materials, Zhangjiang Institute for Advanced Study, Shanghai Jiao Tong University, Shanghai 201203, China

[3]Department of Chemical and Biological Engineering, University at Buffalo, The State University of New York, Buffalo, New York 14260, United States

[4]Department of Materials Science and Engineering and Department of Chemistry, University of Wisconsin–Madison, Madison, Wisconsin 53706, USA

[5]National Key Laboratory of Advanced Micro and Nano Manufacture Technology and Key Laboratory of Polymer Chemistry and Physics of Ministry of Education, School of Materials Science and Engineering, Peking University, Beijing, Beijing 100871, China

*E-mail: kaihangs@buffalo.edu; yaozhenpeng@gmail.com.

Abstract:

Nanoporous materials hold promise for diverse sustainable applications, yet their vast chemical space poses challenges for efficient design. Machine learning offers a compelling pathway to accelerate the exploration, but existing models lack either interpretability or fidelity for elucidating the correlation between crystal geometry and property. Here, we report a three-dimensional periodic space sampling method that decomposes large nanoporous structures into local geometrical sites for combined property prediction and site-wise contribution quantification. Trained with a constructed database and retrieved datasets, our model achieves state-of-the-art accuracy and data efficiency for property prediction on gas storage, separation, and electrical conduction. Meanwhile, this approach enables the interpretation of the prediction and allows for accurate identification of significant local sites for targeted properties. Through identifying transferable high-performance sites across diverse nanoporous frameworks, our model paves the way for interpretable, symmetry-aware nanoporous materials design, which is extensible to other materials, like molecular crystals and beyond.

Introduction

Nanoporous materials, featured by their characteristic pores and voids with diameters varying from several to a hundred nanometers, encompass a diverse family of structures including zeolites, metal-organic frameworks (MOFs), and covalent organic frameworks (COFs). Their intricate network of nanoscale pores, exceptionally high surface areas, and adjustable internal surface properties have emerged as pivotal platforms[1–4] for the development of clean energy applications and beyond, such as catalysis[5–8], gas storage and separation[9,10], advanced energy storage[11–15], sensing[16,17] , ionic conduction,[15,18,19] and drug delivery [20,21]. However, adapting a nanoporous material to meet a specific application is far from straightforward. In the case of MOFs, the design process of a MOF entails selecting suitable metal nodes and organic linkers to self-assemble following a specific topology, and performing a proper post-synthetic treatment.[22–24] To date, more than a hundred different metal nodes and topologies have been reported, and the number of potentially viable linkers has been estimated to be vast.[25,26] Together, these choices define an enormous chemical space for MOF, and more broadly, the nanoporous materials. An effective and efficient exploration of this space thus demands approaches beyond the Edisonian-like trial-and-error method, and data-driven techniques like machine learning offer a promising way.

A competent machine learning workflow in materials science hinges on building a bridge between materials' composition, structure, and resulting properties, which generally starts by converting each material to a numerical representation that a machine learning model can learn from and predict. As a result, machine learning models are often dictated by the choice of representation; for instance, a graph-based encoding naturally leads to a graph neural network[27], whereas a voxelized or image-like representation calls for a convolutional architecture[28]. Just as with other crystalline materials, researchers have developed a variety of representations specifically for nanoporous frameworks, each designed to capture their chemical, physical, and crystallographic information. Descriptor-based representations, such as stoichiometric features[29] and smooth overlap of atomic positions (SOAP)[29] have been proposed for nanoporous materials. These can help reduce input dimensionality and allow the employment of simpler models. Yet, their reliance on precomputed and partial features rather than the full structural detail often limits predictive performance.[30–33] Graph representation has also been applied, but converting the nanoporous structure into a graph will lose the information about its three-dimensional (3-D) conformation, which is critical for accurate prediction of properties like gas adsorption.[29,34]

One notable representation scheme for nanoporous materials is the energy grid-based representations, including the one-dimensional (1-D) energy histogram[35], the two-dimensional (2-D) energy histogram[36], and the 3-D voxel[37–39]. In the 1-D representation creation, the materials structure is gridded, the interaction energy between the material and the probe atom at each grid point is calculated (energy grid), and the energy distribution is then collected as the input. The 2-D variant extends this approach by incorporating energy gradient magnitudes as a second dimension. Both the 1-D and 2-D histograms have shown impressive results for achieving high accuracy with relatively simple regression methods like multilayer perceptron (MLP)[35] and LASSO[36]. The 3-D voxel representations preserve spatial correlations by directly processing raw energy grids through 3-D convolutional neural networks (CNNs), thereby retaining localized geometric features that lower-dimensional projections inherently

discard.[37–39] Yet it is challenging to enforce translational and rotational symmetry with the 3-D voxels, and related models therefore require significantly more data to train[40,41]. While achieving promising prediction accuracy, energy grid-based approaches inevitably obligate energy grid calculations, and the energy grid may appear as an artificial barrier that prevents the researcher from directly linking the performance to localized structural features, causing difficulties in the model's interpretability. Besides, hybrid embeddings (*e.g.*, RFcode) encode the chemically meaningful organic linkers as SMILES[42]/graphs[26] while representing metal nodes and topology with simplified symbolic tokens for better overall efficiency. Hybrid embeddings can be readily processed by recurrent neural network/transformer-based architectures (as demonstrated by SmVAE and MOFormer[26,29,43,44]). However, this convenience comes at the cost of discarding explicit 3-D structural information. To date, incorporating comprehensive structural information into representations for nanoporous materials is still an open challenge.

When dealing with problems like materials design, any model (representation) must respect the symmetries of 3-D space[45–47]. The prediction of the model should change accordingly with the system (*i.e.*, equivariance) when necessary (*e.g.*, vectors like forces), but stay constant (*i.e.*, invariance) under rotational, translational, and inversion transformations (*e.g.*, scalars like molecular identity) when required. As noted above, descriptors that previously enforced these symmetries often sacrificed full structural details. The recent development of equivariant neural networks coupled with 3-D atom graph representations presents an elegant solution to material representation challenges, which inherently ensures these rules through tensor products on spherical harmonic functions.[48–50] Equivariant models enhance data efficiency by incorporating prior knowledge of symmetries, eliminating the need for data augmentation, and speeding up the training and inference process.[51] Additionally, recent work has demonstrated that integrating equivariant layers into a transformer framework can further improve predictive power.[52,53] These architectures have achieved state-of-the-art performance across diverse domains requiring geometric fidelity, including molecular dynamics[52–56], charge density prediction[57,58], accurate formation energy prediction[59], and protein structure prediction[60]. The same geometric deep learning principle should naturally extend to the modeling of nanoporous materials, in which the strength of equivariant networks remains unexplored.

Beyond accuracy, another vital assessment for machine learning models in materials design is their interpretability. In addition to trust and fairness, a worthwhile model should provide mechanistic interpretations or explanations that drive its predictions, ideally, more profound insights into material behaviors at various scales during chemical and physical processes. Ultimately, novel domain knowledge of materials science and straightforward design principles for property-oriented materials design shall be offered.[61–63] Being a topic still in infancy, interpretable machine learning or artificial intelligence (XML or XAI) has drawn notable attention from the materials science modeling field, with several approaches being introduced. Feature importance methods, such as SHAP, can help identify the most influential features in predictions.[64,65] However, these importance numbers can be challenging to interpret when features are correlated or when dealing with complicated problems. Another way to increase model explainability is to select some typical examples from the input, using methods like k-nearest neighbors.[61]

Intuitiveness can be provided by showing similar training samples, but the choice of examples can limit their strength and may not generalize well. Surrogate models approximate complex models with simpler, more interpretable ones, offering a route to interpretability. However, this often comes at the cost of predictive performance, and the choice of the surrogate model is frequently subjective.[66–68] Parameter or intermediate output inspection techniques (*e.g.*, t-SNE and PCA) allow researchers to visualize the model's learned embeddings (*e.g.*, SchNet), offering insights into the data's structure. Still, these visualizations are usually subjective and may not directly lead to actionable understandings.[69–72] Therefore, given the generally limited clarity of materials data, building a machine learning model for materials design with well-balanced predictive power and interpretability is still under investigation.

In this work, we build an equivariant graph network-based model for nanoporous material design with full structural-property interpretability. We develop a 3-D periodic space sampling method that decomposes large nanoporous structures into local geometrical sites for combined property prediction and contribution quantification of each site. This approach enables an interpretation of how the prediction works and allows for the accurate identification of significant local sites influencing the target properties, ultimately bringing new insights to the design of nanoporous materials. To train and test our model, we retrieve all previous databases and build a new binary adsorption dataset on CO_2 and N_2 in CoRE MOFs.[73–75] Our model outperforms state-of-the-art ML models with superior predictive accuracy and data efficacy for exemplified applications (*i.e.*, gas storage, separation, and electrical conduction). Moreover, we demonstrate that our model understands the local geometrical features and clearly establishes the connection between structure and properties. Corresponding strong sites for each targeted application are summarized to guide future property-oriented nanoporous materials design. We make our trained models, results, and code available as open source to aid reproducibility and adoption to broader applications (for example, COFs, metal-organic polyhedra, hydrogen-bonded organic frameworks, and coordination polymers).

Equivariant graph neural networks for interpretable nanoporous materials design

The performances of nanoporous materials are dictated by their multitudinous and complex structures. Just as adsorbate molecules do not distribute uniformly throughout the pores of nanoporous materials, different regions, or local sites, within these materials can contribute very differently to overall performance. For example, open metal sites (OMSs) in MOFs facilitate strong interactions with various molecules and dominate total gas adsorption[76]. Tetrathiafulvalene sites in COFs promote the formation of π-conjugated systems, enabling high electrical conduction[77]. Therefore, identifying the strong performance sites in nanoporous materials is critically essential to obtain the capability to fine-tune those sites, sterically and electronically, for maximized performance output. However, experimental determination of the strong sites is rather challenging due to the limitations of current characterizations in providing adequate structural details of the sites[78,79]. Computational methods such as GCMC and DFT generally demand a relatively large amount of computational resources to obtain[75,80]. Here, we put forward a 3-D spatial sampling strategy-centered algorithm, which can decompose nanoporous structures into their constituent sites and precisely estimate each site's contribution to the overall material performance. Additionally, it partitions the structure to reduce input dimensionality, thereby enhancing

model accuracy and transferability in low-data regimes. By benchmarking the contributions of distinct sites, we can identify superior sites, analyze the factors that make them exceptional, and help determine how to combine them to design advanced nanoporous materials.

As shown in **Fig. 1a-d**, during the sampling process, a detection window (corresponding to a specific site *i*), which is geometrically specified as a sphere with a predetermined radius, will be traversed throughout the unit cell with a uniform real-space step size in three spatial dimensions, ensuring a thorough sampling of the structure. To properly account for the inherent periodicity of crystalline materials, periodic boundary conditions are enforced so that atoms in neighboring cells are incorporated when the window is positioned near a cell boundary. Leveraging an equivariant transformer, our model X(3)mat preserves the integrity of geometry information with no additional preprocessing, as shown in **Fig. 1e**.[53] The atomic coordinates and types from each detection window ($site_i$) are directly input into the equivariant neural network model, which inherently enforces rotational, translational, and inversional invariance for robust, physically consistent feature extraction. Conceptually, the equivariant transformer follows the format of a standard transformer encoder (detailed architecture in **Fig. S1**), with an embedding layer to lift the inputs to latent space, then stacked self-attention blocks capturing the pairwise and higher-order interactions, following a contribution layer to predict the scalar contribution for the specific $site_i$. Within each self-attention block, the fully-connected layers and layer normalization are replaced by equivariant convolutional modules (*i.e.*, eSCN[81]) and equivariant layer normalization. Finally, we achieve combined property prediction and interpretation by constructing the loss function from the site contribution assigned by the model. Here, the overall capacity of a material is yielded by averaging the outputs from all detection windows/sites across the structure, and the training loss is defined as the discrepancy between the actual adsorption capacity and the aggregated prediction for each structure.

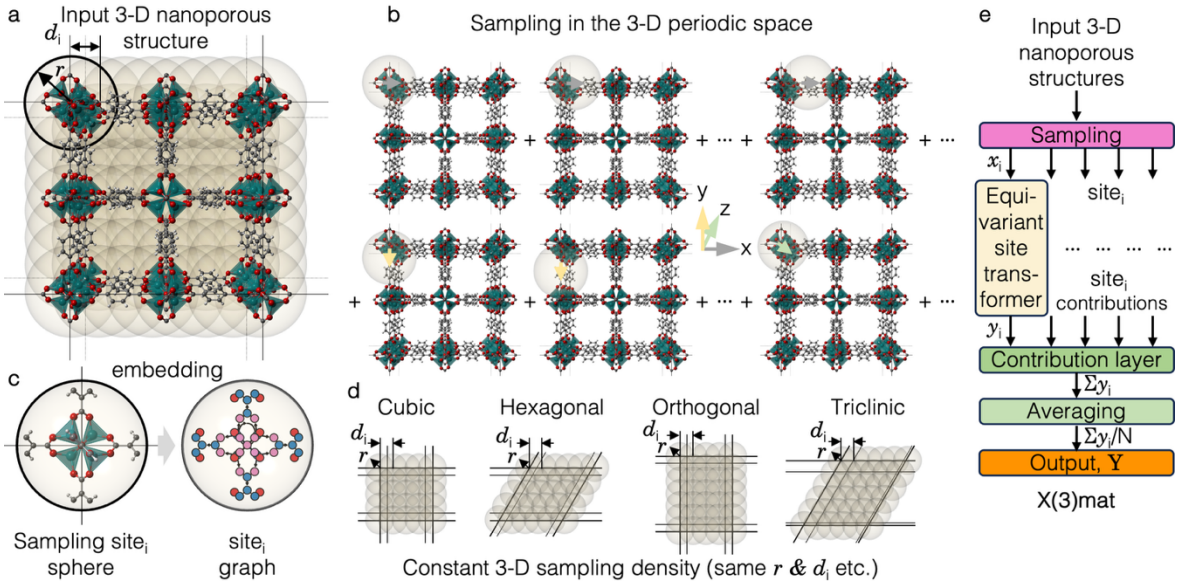

Figure 1. Equivariant graph neural networks for interpretable design of nanoporous materials. a. Arrangement of the detection windows in the exemplified input structure (*e.g.*, MOF-5). **b.** Illustration of the sampling process throughout the input structure. **c.** An example of the sampling site and its encoded 3-D graph inside a detection window. **d.** The

behavior of the sampling process in distinct crystal systems. **e.** Structure of the equivariant graph neural networks X(3)mat for interpretable design of nanoporous materials.

Datasets construction and model training & optimization

We demonstrate our model for three exemplified applications of nanoporous materials (zeolites and MOFs): N_2 adsorption, N_2/CO_2 separation, and electrical conduction. For N_2 adsorption in zeolites, the adsorption value dataset was built using RASPA2[82] with the IZA database[73] . For N_2 adsorption in MOFs, the adsorption capacity data in the CoRE MOF 2019 database[74] were retrieved with properties at 1 bar pressure and 77 K in the isothermal results.[73–75,83] Nanoporous materials are promising for gas separation applications due to their unique properties, such as well-defined pore structures and tunable surface chemistry, enabling precise molecular sieving and selective adsorption[84,85]. However, machine learning applications for gas separation prediction in nanoporous materials were constrained by the lack of high-quality datasets and the general difficulty of mixed gas adsorption computation[26,32]. Accurate prediction of mixed gas adsorption demands that models genuinely capture how each local site in the framework interacts with different gas species, rather than relying on simplified proxies like surface area. Here, we construct our dataset by simulating N_2/CO_2 binary gas adsorption with gRASPA,[86] a graphics processing unit (GPU)-accelerated Monte Carlo software, on CoRE MOF 2019 structures[74], enabling us to evaluate our model performance by discerning the local sites' contributions to the overall separation of two gases.[86] Finally, to assess the model's versatility, we evaluated its capability on bandgap prediction using the retrieved QMOF dataset[75]. Distributions of the four datasets are illustrated in **Fig. S2**. The training and validation sets are partitioned in the ratio of 4:1 and 7:3 for gas adsorption/separation and electrical conduction applications. Among all hyperparameters, detection window (site) radius and sampling step size are critical for capturing the local chemical environment. The window radius must be appropriately set to balance the need for sufficient local chemical information against the risk of unnecessarily increased input dimensionality. An undersized window may fail to encompass the relevant pore and channel accessibility information, while an oversized window could dilute the local features critical to adsorption. To address this, we conduct a convergence test with different window radii (including the whole structure) as input for targeted applications (see **Fig. S3**). Our results indicate that a radius of 6 Å/8 Å is optimal for gas adsorption and band gap prediction. Similarly, the sampling step size is set to 2Å for the trade-off between accuracy and computational cost. Furthermore, to ensure a fair comparison when benchmarking our approach against state-of-the-art machine learning algorithms for nanoporous materials, we use a fixed random seed when partitioning the datasets for all the models, and thoroughly optimize hyperparameters of these reference models with current datasets employing the Optuna library.[87]

Benchmarking against state-of-the-art models and data efficacy

As shown in **Fig. 2** and **Tab. 1**, our model X(3)mat demonstrates outstanding accuracy and robust data efficacy against state-of-the-art models for nanoporous materials (*i.e.*, zeolites and MOFs) across all applications (*i.e.*, N_2 adsorption, N_2/CO_2 separation, and electrical conduction). For zeolite N_2 adsorption prediction (**Fig. 2a,d**), our model leads all other models with a large gap. For MOF N_2 adsorption

prediction, our model is marginally outperformed by the 2-D energy histogram method with four layers MLP (**Fig. 2a,e**), which is fed with extra energetic information from additional calculations. Our model comes back on top when we train all the models with gravimetric properties instead of the volumetric properties (**Tab. S5**). For MOF N_2/CO_2 separation and band gap predictions (**Fig. 2b,c,f-h**), our model once again exhibits superior precision against existing models. Furthermore, we evaluate the data efficacy of our model against current leading methods (*e.g.*, MOFormer[29] and CGCNN[29]). As shown in **Fig. 2i**, our model demonstrates improved data efficiency with dataset sizes from 10^2 to 10^4. We attribute its performance to equivariant networks' capability to reduce the redundant freedoms while preserving the key symmetries, and the usage of the local structure within a detection window as input. Such a dimensionality reduction is particularly advantageous when working with limited sample sizes.

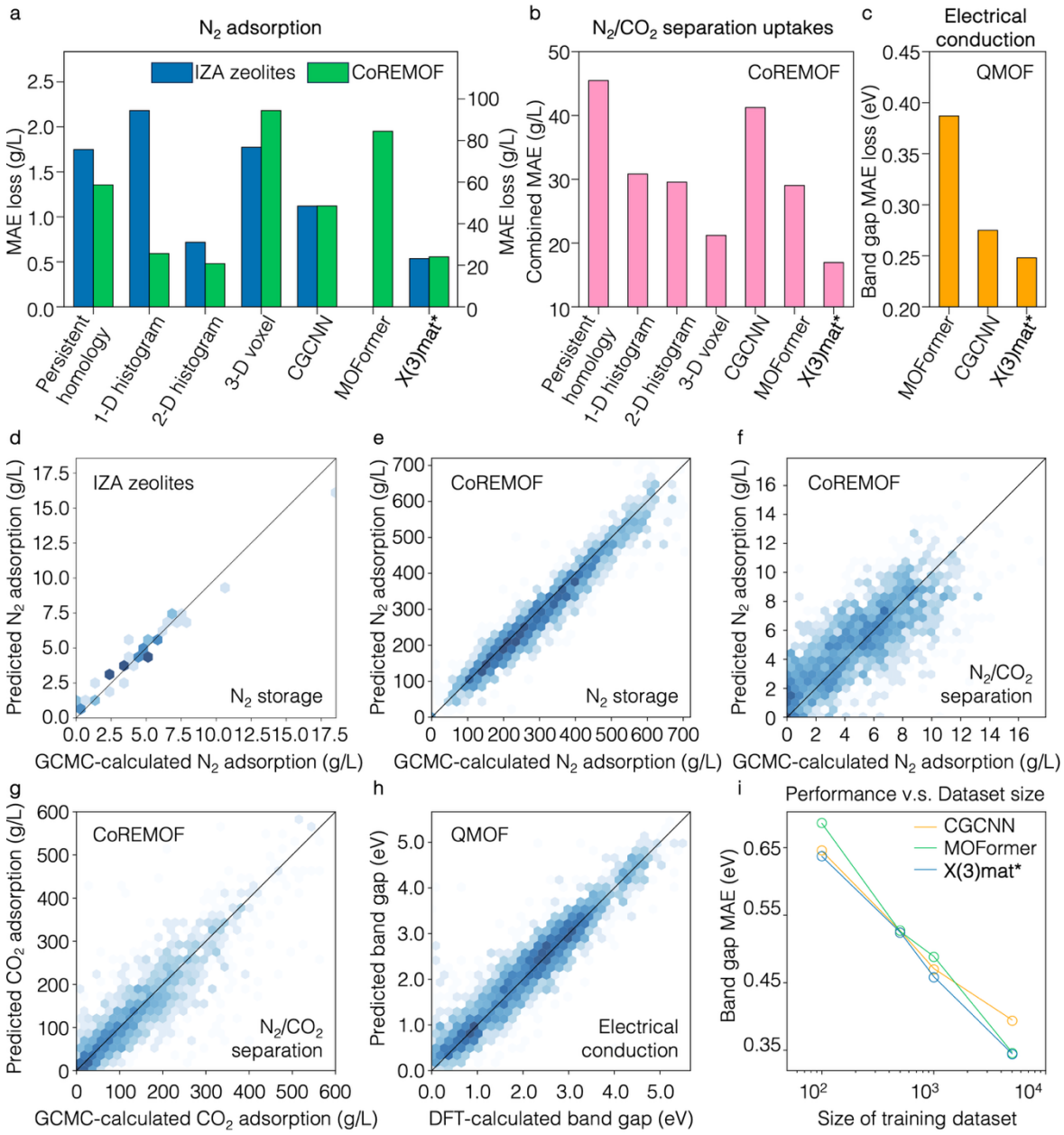

Figure 2. X(3)mat enables efficient and accurate prediction of nanoporous materials properties in exemplified applications. a. The benchmark of N_2 adsorption capacity prediction against state-of-the-art models with the IZA zeolite and MOF 2019 datasets. **b.** The benchmark of N_2/CO_2 separation uptake predictions against state-of-the-art models with

the CoRE MOF 2019 dataset. **c.** The benchmark of band gap prediction against state-of-the-art models with the QMOF dataset. **d.** Predicted N_2 adsorption capacity by X(3)mat against GCMC calculations of the IZA zeolites dataset. **e.** Predicted N_2 adsorption capacity by X(3)mat against GCMC calculations of the CoRE MOF dataset. **f.** Predicted N_2 adsorption capacity by X(3)mat against GCMC calculations of the CoRE MOF CO_2/N_2 separation dataset. **g.** Predicted CO_2 adsorption capacity by X(3)mat against GCMC calculations of the CoRE MOF CO_2/N_2 separation dataset. **h.** Predicted band gap by X(3)mat against DFT calculations of the QMOF dataset. **i.** The benchmark of data efficacy against state-of-the-art models with the QMOF dataset. *This work.

Table 1. Benchmarking against state-of-the-art nanoporous materials models.

	Zeolite N_2 storage MAE (g/L)	MOF N_2 storage MAE (g/L)	MOF N_2/CO_2 average uptake MAE (g/L)	MOF band gap MAE (eV)
Persistent homology[33]	1.75	58.64	45.47	-
1-D energy histogram[35]	2.18	25.62	30.82	-
2-D energy histogram[36]	0.72	**20.77**	29.55	-
3-D voxel[39]	1.77	94.41	21.20	-
CGCNN[29]	1.12	48.54	41.24	0.275
MOFormer[29]	-	76.99	28.12	0.387
X(3)mat*	**0.54**	24.03	**16.95**	**0.248**

*This work

Demonstrating model interpretability in exemplified applications

Gas adsorption and separation

The most prominent feature of our method, in contrast to previous methods, is its ability to detect the local geometries in the structures that contribute to the target property rather than solely predict the overall property value. The output of our model provides a smooth map for illustrating the contributions of all local sites within a nanoporous structure. As shown in **Fig. 3a,b**, overlaying the spatial map of site-wise contributions (y_i) as predicted by our model with the GCMC computed N_2 adsorption density (Y) distribution reveals a pronounced correlation. Using our model, we can assign the adsorption sites ($site_i$) surrounding these high-density zones that are most responsible for the observed N_2 uptake. As shown in **Fig. 3a** and **Fig. S4a**, the cavity wall edges of the large pores in zeolite LTA are flagged by our model as the dominant adsorption sites ($site_i$) with maximized contribution (y_i = 8.84 g/L). The joint effect of two nearby strong adsorption sites brings forward the adsorption density maximum as observed (grey arrows). We can also notice that the contribution maximum point does not align with the adsorption density maximum position, because the cavity walls are dense local geometries and impenetrable to adsorbed N_2 gas. As a result, the adsorption occurs around the site, yet not precisely at the site, and we then define this type of strong contribution site as the "Exterior" type. As a comparison, in **Fig. 3b** and **Fig. S4b**, a pore inside zeolite ASV is identified as the strong contribution site ($site_i$, y_i = 16.83 g/L), which is accessible to N_2 gas, and the center of predicted contributions coincides precisely with the density maximum (grey arrow). We define this type of strong contribution site as the "Interior" type. Both of these types of strong contribution sites will function interchangeably for nanoporous materials, with more examples given for a number of zeolites and MOFs in **Fig. S5.**

For gas separation/mixed-gas adsorption, each site's contributions to CO_2 and N_2 adsorptions are predicted by our model, respectively. Then, the spatial selectivity contribution map can be computed by taking the ratio of these contributions. As shown in **Fig. 3c**, three distinct strong adsorption sites ($site_i$, $site_j$, $site_k$) are identified, which serve as "Exterior" type for both N_2 adsorption ($y_i/y_j/y_k$ = 2.42/2.30/1.23 g/L) and CO_2 adsorption ($y_i/y_j/y_k$ = 396.15/414.10/477.12 g/L). The contribution of N_2 is confined to regions distant from the cage due to its relatively large molecular size. By contrast, CO_2 exhibits strong contributions distributed across the cage, with maxima near the Gd metal nodes. The selectivity maximum of CO_2 over N_2 is then located in the regions with strong CO_2 contribution yet relatively weak N_2 contribution. The whole procedure is visually analogous to "carving out" the strong N_2 contribution regions (black arrows) from the CO_2 contribution map (black arrows+yellow arrows), and the resulting selectivity contribution distribution closely mirrors the ground truth selectivity pattern (orange arrows). The capability of our model in determining the highly selective sites applies universally across the dataset, and more examples are given for another two MOFs in **Figs. S6** and **S7**.

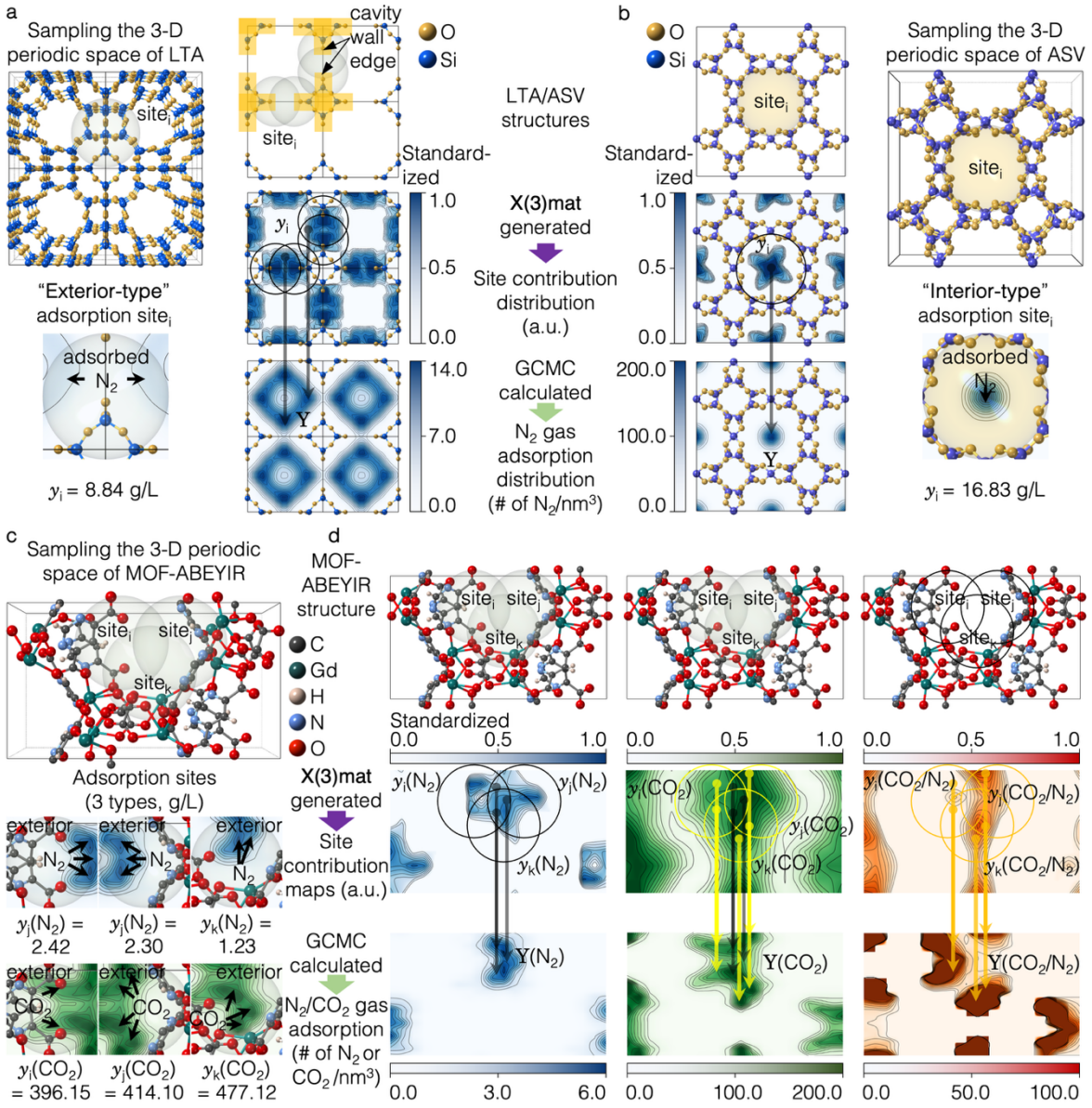

Figure 3. X(3)mat interpretability demonstration in nanoporous materials design for gas adsorption and separation. **a.** Spatial map of site-wise contributions predicted by X(3)mat in zeolite LTA shows pronounced correlation with the GCMC computed N_2 adsorption density distribution. The model flags cavity wall edges as the dominant adsorption sites ($site_i$) with maximized contribution, and the joint effect of two nearby strong sites brings the adsorption density maximum as observed (black arrows). The contribution maximum point does not align with the adsorption density maximum position due to the impenetrability of the wall edges, which is then defined as the "Exterior" type strong adsorption site. **b.** A pore inside zeolite ASV is identified as the strong contribution site, which is accessible to N_2 gas, and the center of predicted contributions coincides precisely with the density maximum (black arrow), which is then defined as the "Interior" type strong adsorption site. **c.** For gas separation, each site's contributions to CO_2 and N_2 adsorptions are predicted by our model, and the spatial selectivity contribution is then computed through ratio calculation. Three distinct strong adsorption sites ($site_i$, $site_j$, $site_k$) are identified, which serve as "Exterior" type for both N_2 and CO_2 adsorption. The selectivity maximum of CO_2 over N_2 is then located in the regions with strong CO_2 contribution yet relatively weak N_2 contribution. The whole procedure is visually analogous to "carving out" the strong N_2 contribution regions (black arrows) from the CO_2 contribution map (black arrows+yellow arrows), and the resulting selectivity contribution distribution closely mirrors the ground truth selectivity pattern (orange arrows).

Electrical conduction

Conductive nanoporous materials (*e.g.*, MOFs and COFs) are intriguing due to their potential to combine the conventional nanoporous materials' merits, such as porosity and tunable chemistry, with electrical conductivity, which makes them promising for a wide range of applications, including energy storage, catalysis, and sensing. Many approaches have been put forward to realize electrical conductivity in nanoporous materials, including networks of coordination bonds for continuous charge delocalization [88,89], extended π−d conjugation crossing the planes[90,91], stacked π−π interaction through the space[92], redox hopping[93], and so on[75,94,95]. However, there is a lack of quantitative tools for the accurate identification of conductive channels/sites and evaluation of their contributions to the overall electrical conductivity, where our model can fill the gap. As shown in **Fig. 4a,b**, deeper blue colors indicate lower band gap contributions, or in other words, higher electrical conduction contribution, in the contribution distribution maps predicted by our model. For the framework with a high band gap (5.11 eV) and low conductivity (**Fig. 4a**), its strong conduction contribution sites barely appear on the acylammonium functional group with a relatively low band gap contribution (y_i = 4.57), corresponding to the slightly delocalized yet isolated electron density around the acylammonium functional group (grey arrow and **Figs. S8a** and **S9a,b**). In contrast, for the MOF with a zero band gap (**Fig. 4b**), the strong conduction sites of the cobalt node exhibit a negative band gap contribution (y_i = −0.40), corresponding to the well delocalized electron density around the bridging enediolate cobalt motif (black arrow). What is more important is that all these strong conduction sites are bridged together in the reticular framework (**Figs. S8b** and **S9c,d**), indicating a continuous electron transport pathway and then a metallic band gap. Another example of using our model for conductive MOF analysis is shown in **Fig. S10**.

Delving further, our model can generate a histogram showing the distribution of local sites with strong, medium, and weak contributions, which will also elucidate the structural origins of their electronic properties. As depicted in **Fig. 4c**, charge conduction in this example structure is mainly from the Co node and the connecting cyclobutanetetrone bridge, which form the charge transport pathway of the structure.

Meanwhile, many high-frequency local sites react against the conduction with positive bandgap contributions. Such a contribution distribution histogram can also be extended for the entire dataset, with an extra axis indicating the real band gap range of all MOF structures. In the plot, a notable peak ridge shows up (along $y = x$), signifying that for all structures sharing a given band gap, their ensemble of site-wise contributions is distributed with its peak precisely at the actual band gap value. Additionally, the region of negative contributions shows the strong sites that act to lower the overall band gap, and these sites are of interest for future conductive MOF design. The area of this region decreases as the real band gap increases. Finally, it disappears when the real band gap approaches around 4.5 eV, indicating the vanishing of local conductive sites in highly dielectric MOFs. The same histograms depicting N_2 contribution distribution in zeolites and MOFs, N_2/CO_2 separation in MOFs, are shown in **Figs. S11**, **S12**, and **S13**, respectively.

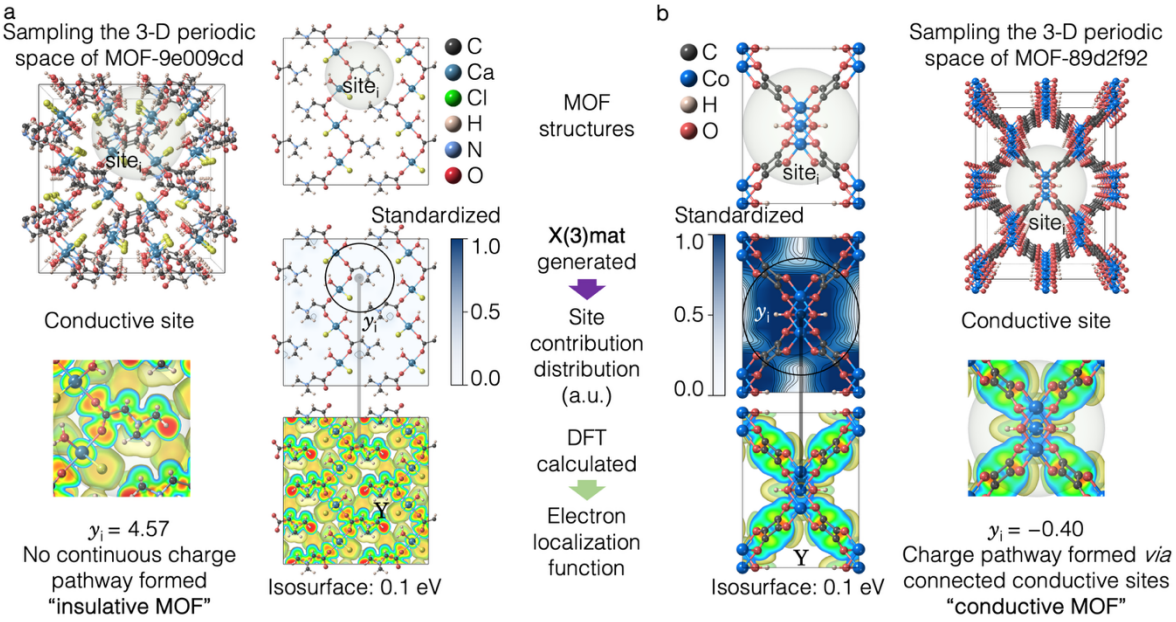

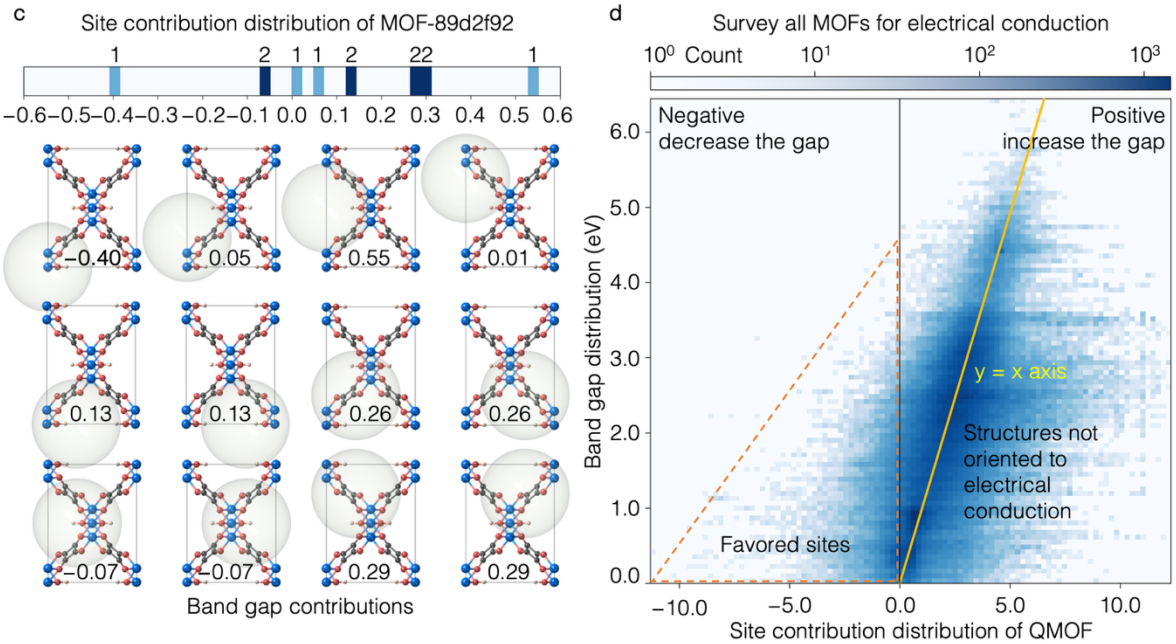

Figure 4. X(3)mat interpretability demonstration in electrical conductive MOF design. a. Comparison between the isosurface mapping calculated by DFT and the site-specific band gap contribution density (higher transparency indicates higher band gap). For a framework with a high band gap (5.11 eV) and low conductivity, its strong conduction contribution sites barely appear on acylammonium functional group with a relatively low band gap contribution (y_i = 4.57), corresponding to the isolated electron density around the acylammonium functional group (grey arrow). **b.** Comparison between the Isosurface mapping calculated by DFT and the site-specific band gap contribution density (higher transparency indicates higher band gap) predicted by the model. For a MOF with a zero band gap, the strong conduction sites of the Co node exhibit a negative band gap contribution (y_i = −0.40), corresponding to the well delocalized electron density around the bridging enediolate cobalt motif (black arrow). All these strong conduction sites are bridged together in the reticular framework, indicating a continuous electron transport pathway and then a metallic band gap. **c.** A histogram shows the distribution of local sites with strong, medium, and weak conduction/band gap contributions, elucidating the structural origins of their electronic properties. **d.** The distribution of site contribution in the entire QMOF dataset against real band gap distributions. A notable peak ridge shows up (along $y = x$), signifying that for all structures sharing a given band gap, their ensemble of site-wise contributions is distributed with its peak precisely at the actual band gap value. Additionally, the region of negative contributions shows the strong sites that act to lower the overall band gap, and these sites are of interest for future conductive MOF design.

Identification of prevalent strong contribution sites and design principles

The rational design of nanoporous materials targeted at specific properties by tuning their local geometries/sites is crucial for various applications. It is then compelling to survey all the existing local geometries and pinpoint the ones that contribute the most to specific applications. Nanoporous materials with improved performance can then be developed, taking advantage of these top candidates. To achieve this goal, we should be able to decompose and distinguish various types of local sites before quantifying their contribution and ranking them subsequently. Our model has demonstrated its capability in decomposing a nanoporous structure and evaluating contributions of the resulting components. How to determine if two sites are identical/distinct, given that all atoms at these sites are in constant vibration, is the problem to solve here. To address this, we eliminate the coordination variables of the atoms and use the graph structure as the identity of the site. For each pair of sites, we compute their Weisfeiler-Lehman (WL) graph hash values[96]. If the hash values match, they are considered the same graph and therefore the same site. For pure silica zeolites, we simplify the comparison by removing the oxygen atoms, while for reticular frameworks, H-removed graphs are used to save computation resources and reduce the complexity of the graph representation while preserving the site's topological information[97].

The top five strong N_2 adsorption sites in the IZA zeolite dataset detected by X(3)mat are presented in **Tab. S1**. For each site, we show the local site structure, average contribution of each strong site, site type, along with the name, structure, and adsorption uptake of an example parent structure. An 8-membered ring (*i.e.*, 8 Si atoms) pore window or a large cage (~9Å diameter) corner with 6-membered ring walls represents an ideal site for N_2 adsorption in zeolites. **Tab. S2** presents the strong adsorption sites identified in the CoRE MOF dataset. Site 1 and Site 2 correspond to an open metal site (OMS) of Zr and Cu surrounded by benzene or pyridine rings. Site 3 is two benzene rings oriented perpendicular to each other near one OMS of Cu. Site 4 is an OMS of Zn forming a plate. The plate-like local structures with hollow regions perpendicular to them can serve as decent landing sites for the adsorbate, and

therefore significantly increase the adsorption contributions. Site 5 is an OMS of Mg connected by a benzene ring stacked over another benzene ring. All these top sites confirm the dominance of OMS upon N_2 adsorption, while sites 3 and 5 highlight the significant role of benzene rings in nitrogen adsorption under 1 bar pressure[98]. The top 5 CO_2-selective sites are shown in **Tab. S3**. Site 1 is an OMS of Zr metal sites connected with multiple benzene ring linkers. Similarly, site 5 in Mg-MOF-74 (CCDC code: VOGTIV) consists of two groups of Mg metal sites connected together, which has been reported by Britt et al. as a well-known CO_2 strong selective capture site owing to the intrinsic binding nature of the open metal centers[99]. Site 2 also corresponds to a CO_2 selective adsorption site in a representative reported structure[100], attributable to the presence of abundant amino groups. These $–NH_2$ moieties, together with their appended amine functionalities, significantly enhance CO_2 selectivity by functioning as Lewis base centers and providing the hydrogen bonding to oxygen atoms of CO_2. Site 3 corresponds to the Co metal center, from which the linkers bearing phenyl rings extend outward in four directions. Site 4 is a pore enclosed by C–N heterocycle linkers and Eu metal nodes. This pore of limited size selectively excludes the N_2 molecules, yet accommodates the adsorption of the smaller CO_2 molecules[101]. In addition, the attraction exerted by the Eu nodes further enhances the high CO_2 selectivity observed at this site. The top five conductive sites as identified are shown in **Tab. S4**. Sites 1 form conductive pathways through the stacking heterocyclic rings composed of carbon and nitrogen atoms. It highlights that nitrogen-substituted aromatic linkers, such as triazine, offer intrinsic advantages over simple benzene rings by promoting extended π-conjugation, enforcing geometric planarity[102], and enhancing π-acidity[94,103], thereby strengthening charge transport *via* both π–d conjugation and π–π stacking pathways. Meanwhile, sites 2, 3, and 5 highlight the advantage of M–N coordination (pyrazolate/iminyl/diamine donors) over M–O (carboxylate/phenolate) for electronic transport in MOFs. Compared to the relatively hard O donors, softer N donors afford greater metal–ligand covalency and better energy matching with aromatic π-orbitals, yielding dispersive bands and higher carrier densities[95]. Sites 4 and 6 are large, coplanar fused aromatics. They maximize both the through-bond conjugation across the metal–linker lattice and the through-space π–π overlap between stacked sheets, thereby broadening bands and shrinking transport gaps[104,105]. All these top contribution sites can then be employed for the design of advanced nanoporous materials targeted at diversified applications.

Conclusions

We develop an equivariant graph network model for designing nanoporous materials with full interpretability. We introduce a 3-D periodic space sampling technique that breaks down large nanoporous structures into local geometric sites to predict properties and quantify each site's contribution. This method provides clear insights into the prediction process and enables precise identification of key local sites for specific properties, offering new perspectives for nanoporous material design. We compile a new dataset on CO_2 and N_2 separation in CoRE MOFs, alongside existing databases, to train and evaluate our model. Our approach surpasses state-of-the-art algorithms for nanoporous materials, achieving higher predictive accuracy and data efficiency in applications such as gas storage, separation, and electrical conduction. Since our sampling method and model can be effortlessly extended to a broader range of

other material systems beyond nanoporous frameworks, it is a fundamental way to advance interpretable machine learning models in materials science.

Methods

1. Hyperparameter optimization of the reference models

Exact model architectures of the prior studies are retrieved from the original papers. MLP models were employed to reproduce the previous persistent homology, 2-D energy histogram, and 1-D energy histogram approaches' results. The energy bin width and energy range are kept the same as the original paper for producing the 1-D and 2-D energy histograms, which are 2 kJ/mol and -30~0 kJ/mol, respectively. The gradient bin width and gradient bin width are 25 kJ/mol/Å and 0~150 kJ/mol/Å, respectively. Layer numbers of the MLP are fixed to 4 for the persistent homology and 2-D model, following previous studies[32,36]. Layer number for the 1-D model is treated as a tunable hyperparameter, because such a low-dimensional representation could result in overfitting given the large number of model parameters in the MLP[35]. To reproduce the 3-D voxel method results, the 3-D convolution ResNet is employed as in the original study[39]. Hyperparameters of these models and the CGCNN model[29] (*e.g.*, neuron amount, convolution layer amounts, learning rate, etc.) are fully optimized *via* the TPESampler algorithm implemented by optuna[87,106] . Notably, MOFormer's hyperparameters were not re-tuned. Instead, we reused the pretrained model checkpoint from the self-supervised training provided by the authors[29].

2. Open dataset construction for MOF N_2/CO_2 separation

The adsorption capacity of CO_2/N_2 binary mixture in MOFs was calculated using grand canonical Monte Carlo (GCMC) simulations using the gRASPA software (version 2025-Mar09).[86] Crystal structures of CoRE MOF 2019 were downloaded from the MOFX-DB database.[83,107] Structures containing extra-framework ions were removed from the dataset. To implement a generalized workflow that retrieves the crystal structures from a database, we developed a Python package, namely gRASPA_job_tracker (version 2025-06-23). The details of this package are discussed in the **Supplementary Notes**. During the simulation, non-bonded interactions were modeled using the Lennard-Jones (LJ) potential with a 12.8 Å cutoff and Lorentz–Berthelot combining rules. Universal force field (UFF) parameters were applied to MOF atoms, while CO_2 and N_2 were treated using the TraPPE force field.[108–110] Long-range electrostatics were computed *via* Ewald summation with a precision of 1×10^{-6}.[111,112] Partial atomic charges for MOFs were predicted by the PACMOF2-neutral machine learning model (DDEC6-based), and those for adsorbates were taken from TraPPE.[113,114] [109] Complete information about the simulation can be found in the **Supplementary Notes A**. Notably, we aim to ensure reproducibility by defining all the required simulation parameters and loading dependencies through a centralized configuration file, which is discussed in **Supplementary Notes** and must be available with any dataset generated from gRASPA_job_tracker.

3. Nanoporous materials electronic structure calculations from first principles

Density functional theory (DFT) calculations were conducted using Vienna Ab initio Simulation Package (VASP)[115] version 5.4.4. The Perdew-Burke-Ernzerhof (PBE)[116] exchange-correlation

functional within the Generalized Gradient Approximation (GGA)[116] was employed for its computational efficiency and reliability. Projector-augmented wave (PAW) pseudopotentials, as recommended for VASP v.5.4.4, were used for all elements[117,118]. A plane-wave energy cutoff of 550 eV was applied, and all calculations were spin-polarized. We used VASPKIT[119] to set up the calculations with the Monkhorst-Pack k-point grids and a density of 0.03 to ensure adequate sampling of the Brillouin zone.

Data availability

Data for the training of the X(3)mat, including the dataset and GCMC movies, are available at zenodo with DOI: 10.5281/zenodo.17151822.

Code availability

Code for the X(3)mat is available at https://github.com/zhenpengyao/X3MAT.

References

1. Zhou, H.-C., Long, J. R. & Yaghi, O. M. Introduction to metal-organic frameworks. *Chem. Rev.* **112**, 673–674 (2012).

2. Furukawa, H., Cordova, K. E., O'Keeffe, M. & Yaghi, O. M. The chemistry and applications of metal-organic frameworks. *Science* **341**, 1230444 (2013).

3. Bennett, T. D., Coudert, F.-X., James, S. L. & Cooper, A. I. The changing state of porous materials. *Nature Materials* **20**, 1179–1187 (2021).

4. Li, Y. & Yu, J. Emerging applications of zeolites in catalysis, separation and host–guest assembly. *Nature Reviews Materials* **6**, 1156–1174 (2021).

5. Zhao, M. *et al.* Metal–organic frameworks as selectivity regulators for hydrogenation reactions. *Nature* **539**, 76–80 (2016).

6. Jagadeesh, R. V. *et al.* MOF-derived cobalt nanoparticles catalyze a general synthesis of amines. *Science* **358**, 326–332 (2017).

7. Lin, S. *et al.* Covalent organic frameworks comprising cobalt porphyrins for catalytic CO2 reduction in water. *Science* **349**, 1208–1213 (2015).

8. Diercks, C. S., Liu, Y., Cordova, K. E. & Yaghi, O. M. The role of reticular chemistry in the design of CO2 reduction catalysts. *Nature Materials* **17**, 301–307 (2018).

9. Zhou, S. *et al.* Asymmetric pore windows in MOF membranes for natural gas valorization. *Nature* **606**, 706–712 (2022).

10. Knebel, A. & Caro, J. Metal-organic frameworks and covalent organic frameworks as disruptive membrane materials for energy-efficient gas separation. *Nature nanotechnology* **17**, (2022).

11. Bai, S., Liu, X., Zhu, K., Wu, S. & Zhou, H. Metal–organic framework-based separator for lithium–sulfur batteries. *Nature Energy* **1**, 1–6 (2016).

12. Sheberla, D. *et al.* Conductive MOF electrodes for stable supercapacitors with high areal capacitance. *Nature Materials* **16**, 220–224 (2016).

13. Bai, S. *et al.* Permselective metal–organic framework gel membrane enables long-life cycling of rechargeable organic batteries. *Nature Nanotechnology* **16**, 77–84 (2020).

14. Shi, R. *et al.* Nitrogen-rich covalent organic frameworks with multiple carbonyls for high-performance sodium batteries. *Nature Communications* **11**, 1–10 (2020).

15. Chi, X. *et al.* A highly stable and flexible zeolite electrolyte solid-state Li-air battery. *Nature* **592**, 551–557 (2021).

16. Kreno, L. E. *et al.* Metal–Organic Framework Materials as Chemical Sensors. **112**, 1105–1125 (2011).

17. Das, G. *et al.* Fluorescence turn on amine detection in a cationic covalent organic framework. *Nature Communications* **13**, 1–12 (2022).

18. Shimizu, G. K. H., Taylor, J. M. & Kim, S. Chemistry. Proton conduction with metal-organic frameworks. *Science* **341**, 354–355 (2013).

19. Yang, J. *et al.* Oxygen- and proton-transporting open framework ionomer for medium-temperature fuel cells. *Science* **385**, 1115–1120 (2024).

20. Abánades Lázaro, I. *et al.* Metal–organic frameworks for biological applications. *Nature Reviews Methods Primers* **4**, 1–20 (2024).

21. Horcajada, P. *et al.* Porous metal–organic-framework nanoscale carriers as a potential platform for drug delivery and imaging. *Nature Materials* **9**, 172–178 (2009).

22. Boyd, P. G. *et al.* Data-driven design of metal–organic frameworks for wet flue gas CO2 capture. *Nature* **576**, 253–256 (2019).

23. Moghadam, P. Z., Chung, Y. G. & Snurr, R. Q. Progress toward the computational discovery of new metal–organic framework adsorbents for energy applications. *Nature Energy* **9**, 121–133 (2024).

24. Diercks, C. S. & Yaghi, O. M. The atom, the molecule, and the covalent organic framework. *Science* **355**, eaal1585 (2017).

25. Kirkpatrick, P. & Ellis, C. Chemical space. *Nature* **432**, 823–823 (2004).

26. Yao, Z. *et al.* Inverse design of nanoporous crystalline reticular materials with deep generative models. *Nature Machine Intelligence* **3**, 76–86 (2021).

27. Xie, T. & Grossman, J. C. Crystal graph convolutional neural networks for an accurate and interpretable prediction of material properties. *Phys. Rev. Lett.* **120**, (2018).

28. Maturana, D. & Scherer, S. VoxNet: A 3D Convolutional Neural Network for real-time object recognition. in *2015 IEEE/RSJ International Conference on Intelligent Robots and Systems (IROS)* (IEEE, 2015). doi:10.1109/iros.2015.7353481.

29. Cao, Z., Magar, R., Wang, Y. & Farimani, A. B. MOFormer: Self-Supervised Transformer Model for Metal–Organic Framework Property Prediction. *Journal of the American Chemical Society* **145**, 2958–2967 (2023).

30. Burner, J. *et al.* High-performing deep learning regression models for predicting low-pressure CO_2 adsorption properties of metal–organic frameworks. *J. Phys. Chem. C Nanomater. Interfaces* **124**, 27996–28005 (2020).

31. Moghadam, P. Z. *et al.* Structure-mechanical stability relations of metal-organic frameworks via machine learning. *Matter* **1**, 219–234 (2019).

32. Krishnapriyan, A. S., Montoya, J., Haranczyk, M., Hummelshøj, J. & Morozov, D. Machine learning with persistent homology and chemical word embeddings improves prediction accuracy and interpretability in metal-organic frameworks. *Scientific Reports* **11**, 1–11 (2021).

33. Park, J. H. *et al.* Superacid counteranion as flexible-coordinating ligand for asymmetric organo-bismuth catalysis. *Nature Communications* **16**, 1–13 (2025).

34. Wang, R., Zhong, Y., Bi, L., Yang, M. & Xu, D. Accelerating Discovery of Metal-Organic Frameworks for Methane Adsorption with Hierarchical Screening and Deep Learning. *ACS Appl Mater Interfaces* **12**, 52797–52807 (2020).

35. Bucior, B. J. *et al.* Energy-based descriptors to rapidly predict hydrogen storage in metal–organic frameworks. *Molecular Systems Design & Engineering* **4**, 162–174 (2019).

36. Shi, K. *et al.* Two-Dimensional Energy Histograms as Features for Machine Learning to Predict Adsorption in Diverse Nanoporous Materials. *Journal of Chemical Theory and Computation* **19**, 4568–4583 (2023).

37. Cho, E. H. & Lin, L.-C. Nanoporous Material Recognition via 3D Convolutional Neural Networks: Prediction of Adsorption Properties. *The Journal of Physical Chemistry Letters* **12**, 2279–2285 (2021).

38. Hung, T.-H., Xu, Z.-X., Kang, D.-Y. & Lin, L.-C. Chemistry-encoded convolutional neural networks for predicting gaseous adsorption in porous materials. *J. Phys. Chem. C Nanomater. Interfaces* **126**, 2813–2822 (2022).

39. Sarikas, A. P., Gkagkas, K. & Froudakis, G. E. Gas adsorption meets deep learning: voxelizing the potential energy surface of metal-organic frameworks. *Scientific Reports* **14**, 1–8 (2024).

40. Musil, F. *et al.* Physics-Inspired Structural Representations for Molecules and Materials. *Chem Rev* **121**, 9759–9815 (2021).

41. Damewood, J. *et al.* Representations of materials for machine learning. *Annu. Rev. Mater. Res.* **53**, 399–426 (2023).

42. Bucior, B. J. *et al.* Identification schemes for metal–organic frameworks to enable rapid search and cheminformatics analysis. *Cryst. Growth Des.* **19**, 6682–6697 (2019).

43. Kang, Y., Park, H., Smit, B. & Kim, J. A multi-modal pre-training transformer for universal transfer learning in metal–organic frameworks. *Nature Machine Intelligence* **5**, 309–318 (2023).

44. Kang, Y. & Kim, J. ChatMOF: an artificial intelligence system for predicting and generating metal-organic frameworks using large language models. *Nature Communications* **15**, 1–13 (2024).

45. Cohen, T. S. & Welling, M. Group equivariant convolutional networks. Preprint at arXiv:1602.07576 (2016).

46. Esteves, C., Allen-Blanchette, C., Makadia, A. & Daniilidis, K. Learning SO(3) equivariant representations with spherical CNNs. in *Computer Vision – ECCV 2018* 54–70 (Springer International Publishing, Cham, 2018).

47. Weiler, M., Geiger, M., Welling, M., Boomsma, W. & Cohen, T. S. 3D steerable CNNs: learning rotationally equivariant features in volumetric data. Preprint at arXiv:1807.02547 (2018).

48. Thomas, N. et al. Tensor field networks: rotation- and translation-equivariant neural networks for 3D point clouds. Preprint at arXiv:1802.08219 (2018).

49. Weiler, M., Geiger, M., Welling, M., Boomsma, W. & Cohen, T. S. 3D Steerable CNNs: Learning Rotationally Equivariant Features in Volumetric Data. *Advances in Neural Information Processing Systems* **31**, (2018).

50. Kondor, R., Lin, Z. & Trivedi, S. Clebsch–Gordan Nets: a Fully Fourier Space Spherical Convolutional Neural Network. *Advances in Neural Information Processing Systems* **31**, (2018).

51. Geiger, M. & Smidt, T. e3nn: Euclidean neural networks. Preprint at arXiv:2207.09453 (2022).

52. Liao, Y.-L. & Smidt, T. Equiformer: equivariant graph attention transformer for 3D atomistic graphs. Preprint at arXiv:2206.11990 (2022).

53. Liao, Y.-L., Wood, B., Das, A. & Smidt, T. EquiformerV2: improved equivariant transformer for scaling to higher-degree representations. Preprint at arXiv:2306.12059 (2023).

54. Gasteiger, J., Becker, F. & Günnemann, S. GemNet: Universal Directional Graph Neural Networks for Molecules. *Advances in Neural Information Processing Systems* **34**, 6790–6802 (2021).

55. Batzner, S. *et al.* E(3)-equivariant graph neural networks for data-efficient and accurate interatomic potentials. *Nature Communications* **13**, 1–11 (2022).

56. Batatia, I. *et al.* The design space of E(3)-equivariant atom-centred interatomic potentials. *Nature Machine Intelligence* **7**, 56–67 (2025).

57. Tang, Z. *et al.* A deep equivariant neural network approach for efficient hybrid density functional calculations. *Nature Communications* **15**, 1–9 (2024).

58. Qiao, Z. *et al.* Informing geometric deep learning with electronic interactions to accelerate quantum chemistry. *Proceedings of the National Academy of Sciences* **119**, e2205221119 (2022).

59. Gong, X. *et al.* General framework for E(3)-equivariant neural network representation of density functional theory Hamiltonian. *Nature Communications* **14**, 1–10 (2023).

60. Jumper, J. *et al.* Highly accurate protein structure prediction with AlphaFold. *Nature* **596**, 583–589 (2021).

61. Zhong, X. *et al.* Explainable machine learning in materials science. *npj Computational Materials* **8**, 1–19 (2022).

62. Burkart, N. & Huber, M. F. A Survey on the Explainability of Supervised Machine Learning. *jair* **70**, 245–317 (2021).

63. Gilpin, L. H. *et al.* Explaining explanations: An overview of interpretability of machine learning. in *2018 IEEE 5th International Conference on Data Science and Advanced Analytics (DSAA)* (IEEE, 2018). doi:10.1109/dsaa.2018.00018.

64. Hartono, N. T. P. *et al.* How machine learning can help select capping layers to suppress perovskite degradation. *Nat. Commun.* **11**, 4172 (2020).

65. Yang, C. *et al.* A machine learning-based alloy design system to facilitate the rational design of high entropy alloys with enhanced hardness. *Acta Mater.* **222**, 117431 (2022).

66. Iquebal, A. S., Pandagare, S. & Bukkapatnam, S. Learning acoustic emission signatures from a nanoindentation-based lithography process: Towards rapid microstructure characterization. *Tribol. Int.* **143**, 106074 (2020).

67. Raccuglia, P. *et al.* Machine-learning-assisted materials discovery using failed experiments. *Nature* **533**, 73–76 (2016).

68. Giles, S. A., Sengupta, D., Broderick, S. R. & Rajan, K. Machine-learning-based intelligent framework for discovering refractory high-entropy alloys with improved high-temperature yield strength. *Npj Comput. Mater.* **8**, (2022).

69. Cecen, A., Dai, H., Yabansu, Y. C., Kalidindi, S. R. & Song, L. Material structure-property linkages using three-dimensional convolutional neural networks. *Acta Mater.* **146**, 76–84 (2018).

70. Schütt, K. T., Sauceda, H. E., Kindermans, P.-J., Tkatchenko, A. & Müller, K.-R. SchNet - A deep learning architecture for molecules and materials. *J. Chem. Phys.* **148**, 241722 (2018).

71. Jha, D. *et al.* ElemNet: Deep learning the chemistry of materials from only elemental composition. *Sci. Rep.* **8**, 17593 (2018).

72. Wang, A. Y.-T., Kauwe, S. K., Murdock, R. J. & Sparks, T. D. Compositionally restricted attention-based network for materials property predictions. *Npj Comput. Mater.* **7**, (2021).

73. Database of Zeolite Structures. https://www.iza-structure.org/databases/.

74. Chung, Y. G. *et al.* Advances, updates, and analytics for the computation-ready, experimental metal–organic framework database: CoRE MOF 2019. *J. Chem. Eng. Data* **64**, 5985–5998 (2019).

75. Rosen, A. S. *et al.* Machine learning the quantum-chemical properties of metal–organic frameworks for accelerated materials discovery. *Matter* **4**, 1578–1597 (2021).

76. Rowsell, J. L. C., Spencer, E. C., Eckert, J., Howard, J. A. K. & Yaghi, O. M. Gas adsorption sites in a large-pore metal-organic framework. *Science* **309**, 1350–1354 (2005).

77. Xie, L. S., Alexandrov, E. V., Skorupskii, G., Proserpio, D. M. & Dincă, M. Diverse π-π stacking motifs modulate electrical conductivity in tetrathiafulvalene-based metal-organic frameworks. *Chem. Sci.* **10**, 8558–8565 (2019).

78. Ezenwa, S. & Gounder, R. Advances and challenges in designing active site environments in zeolites for Brønsted acid catalysis. *Chem. Commun. (Camb.)* **60**, 12118–12143 (2024).

79. Uzun, A. & Keskin, S. Site characteristics in metal organic frameworks for gas adsorption. *Prog. Surf. Sci.* **89**, 56–79 (2014).

80. Wang, T. *et al.* Molecular simulation of gas adsorption in shale nanopores: A critical review. *Renew. Sustain. Energy Rev.* **149**, 111391 (2021).

81. Passaro, S. & Zitnick, C. L. Reducing SO(3) convolutions to SO(2) for efficient equivariant GNNs. Preprint at arXiv:2302.03655 (2023).

82. Dubbeldam, D., Calero, S., Ellis, D. E. & Snurr, R. Q. RASPA: molecular simulation software for adsorption and diffusion in flexible nanoporous materials. *Mol. Simul.* **42**, 81–101 (2016).

83. Bobbitt, N. S. *et al.* MOFX-DB: An online database of computational adsorption data for nanoporous materials. *J. Chem. Eng. Data* **68**, 483–498 (2023).

84. Rodenas, T. *et al.* Metal-organic framework nanosheets in polymer composite materials for gas separation. *Nat. Mater.* **14**, 48–55 (2015).

85. Gu, C. *et al.* Design and control of gas diffusion process in a nanoporous soft crystal. *Science* **363**, 387–391 (2019).

86. Li, Z. *et al.* Efficient Implementation of Monte Carlo Algorithms on Graphical Processing Units for Simulation of Adsorption in Porous Materials. *J Chem Theory Comput* **20**, 10649–10666 (2024).

87. Akiba, T., Sano, S., Yanase, T., Ohta, T. & Koyama, M. Optuna: a next-generation hyperparameter optimization framework. Preprint at arXiv:1907.10902 (2019).

88. Park, J. G. *et al.* Charge delocalization and bulk electronic conductivity in the mixed-valence metal-organic framework Fe(1,2,3-triazolate)2(BF4) x. *J. Am. Chem. Soc.* **140**, 8526–8534 (2018).

89. Gándara, F. *et al.* Porous, conductive metal-triazolates and their structural elucidation by the charge-flipping method. *Chemistry* **18**, 10595–10601 (2012).

90. Day, R. W. *et al.* Single crystals of electrically conductive two-dimensional metal-organic frameworks: Structural and electrical transport properties. *ACS Cent. Sci.* **5**, 1959–1964 (2019).

91. Mähringer, A. *et al.* Oriented thin films of electroactive triphenylene catecholate-based two-dimensional metal-organic frameworks. *ACS Nano* **13**, 6711–6719 (2019).

92. Clough, A. J. *et al.* Metallic conductivity in a two-dimensional cobalt dithiolene metal-organic framework. *J. Am. Chem. Soc.* **139**, 10863–10867 (2017).

93. Ahrenholtz, S. R., Epley, C. C. & Morris, A. J. Solvothermal preparation of an electrocatalytic metalloporphyrin MOF thin film and its redox hopping charge-transfer mechanism. *J. Am. Chem. Soc.* **136**, 2464–2472 (2014).

94. Xie, L. S., Skorupskii, G. & Dincă, M. Electrically Conductive Metal-Organic Frameworks. *Chem Rev* **120**, 8536–8580 (2020).

95. Johnson, E. M., Ilic, S. & Morris, A. J. Design Strategies for Enhanced Conductivity in Metal-Organic Frameworks. *ACS Cent Sci* **7**, 445–453 (2021).

96. Computational Biology Research Group. Weisfeiler-Lehman Graph Kernels. https://jmlr.csail.mit.edu/papers/volume12/shervashidze11a/shervashidze11a.pdf (2011).

97. O'Shaughnessy, M. *et al.* Porous isoreticular non-metal organic frameworks. *Nature* **630**, 102–108 (2024).

98. Gwardiak, S., Szczęśniak, B., Choma, J. & Jaroniec, M. Benzene adsorption on synthesized and commercial metal–organic frameworks. *J. Porous Mater.* **26**, 775–783 (2019).

99. Britt, D., Furukawa, H., Wang, B., Glover, T. G. & Yaghi, O. M. Highly efficient separation of carbon dioxide by a metal-organic framework replete with open metal sites. *Proc. Natl. Acad. Sci. U. S. A.* **106**, 20637–20640 (2009).

100. Vaidhyanathan, R., Iremonger, S. S., Dawson, K. W. & Shimizu, G. K. H. An amine-functionalized metal organic framework for preferential CO(2) adsorption at low pressures. *Chem. Commun. (Camb.)* 5230–5232 (2009).

101. Deng, Z. & Sarkisov, L. Multi-scale computational design of metal–organic frameworks for carbon capture using machine learning and multi-objective optimization. *Chem. Mater.* **36**, 9806–9821 (2024).

102. Klinkebiel, A., Beyer, O., Malawko, B. & Lüning, U. Elongated and substituted triazine-based tricarboxylic acid linkers for MOFs. *Beilstein J. Org. Chem.* **12**, 2267–2273 (2016).

103. Bashiri, R. *et al.* Discovery of dual ion-electron conductivity of metal-organic frameworks via machine learning-guided experimentation. *Chem. Mater.* **37**, 1143–1153 (2025).

104. Wang, J. *et al.* Superior charge transport in Ni-diamine conductive MOFs. *J. Am. Chem. Soc.* **146**, 20500–20507 (2024).

105. Sheberla, D. *et al.* High electrical conductivity in Ni_3(2,3,6,7,10,11-hexaiminotriphenylene)$_2$, a semiconducting metal-organic graphene analogue. *J. Am. Chem. Soc.* **136**, 8859–8862 (2014).

106. Watanabe, S. Tree-structured Parzen estimator: understanding its algorithm components and their roles for better empirical performance. Preprint at arXiv:2304.11127 (2023).

107. https://mof.tech.northwestern.edu/rails/active_storage/blobs/redirect/eyJfcmFpbHMiOnsibWVzc2FnZSI6IkJBaHBHdz09IiwiZXhwIjpudWxsLCJwdXIiOiJibG9iX2lkIn19--b1e93265962e2ec5eec5f34c5da952929bf21a2a/CoREMOF-N2.zip.

108. Rappe, A. K., Casewit, C. J., Colwell, K. S., Goddard, W. A., III & Skiff, W. M. UFF, a full periodic table force field for molecular mechanics and molecular dynamics simulations. *J. Am. Chem. Soc.* **114**, 10024–10035 (1992).

109. Zhang, L. & Siepmann, J. I. Direct calculation of Henry's law constants from Gibbs ensemble Monte Carlo simulations: nitrogen, oxygen, carbon dioxide and methane in ethanol. *Theor. Chem. Acc.* **115**, 391–397 (2006).

110. Potoff, J. J. & Siepmann, J. I. Vapor–liquid equilibria of mixtures containing alkanes, carbon dioxide, and nitrogen. *AIChE J.* **47**, 1676–1682 (2001).

111. Gans, R. & Loyarte, R. G. Die Permeabilität des Nickels für schnelle elektrische Schwingungen. *Ann. Phys.* **369**, 209–249 (1921).

112. Allen, M. P. & Tildesley, D. J. *Computer Simulation of Liquids*. (Oxford University Press, London, England, 2017).

113. Pham, T. D., Joodaki, F., Formalik, F. & Snurr, R. Q. Predicting partial atomic charges in metal–organic frameworks: An extension to ionic MOFs. *J. Phys. Chem. C Nanomater. Interfaces* **128**, 17165–17182 (2024).

114. Kancharlapalli, S., Gopalan, A., Haranczyk, M. & Snurr, R. Q. Fast and accurate machine learning strategy for calculating partial atomic charges in metal-organic frameworks. *J. Chem. Theory Comput.* **17**, 3052–3064 (2021).

115. Kresse, G. & Furthmüller, J. Efficient iterative schemes for ab initio total-energy calculations using a plane-wave basis set. *Phys. Rev. B Condens. Matter* **54**, 11169–11186 (1996).

116. Perdew, J. P., Burke, K. & Ernzerhof, M. Generalized gradient approximation made simple. *Phys. Rev. Lett.* **77**, 3865–3868 (1996).

117. Kresse, G. & Joubert, D. From ultrasoft pseudopotentials to the projector augmented-wave method. *Phys. Rev. B Condens. Matter* **59**, 1758–1775 (1999).

118. Blöchl, P. E. Projector augmented-wave method. *Phys. Rev. B Condens. Matter* **50**, 17953–17979 (1994).

119. Wang, V., Xu, N., Liu, J.-C., Tang, G. & Geng, W.-T. VASPKIT: A user-friendly interface facilitating high-throughput computing and analysis using VASP code. *Comput. Phys. Commun.* **267**, 108033 (2021).

Acknowledgements

Z.Y. and Z.Z. were supported by the National Natural Science Foundation of China (grant number 52373228). Z.Y. and K.S. thank Prof. Andrew Rosen for helpful discussions on the K.S. thanks Dr. Zhao Li for beneficial discussions on the gRASPA software. K.S acknowledges the partial support from the ACS Petroleum Research Fund under Doctoral New Investigator Grant 68604-DNI6. This work used the Delta system at the National Center for Supercomputing Applications through allocation CHM240039 from the Advanced Cyberinfrastructure Coordination Ecosystem: Services & Support (ACCESS) program, which is supported by National Science Foundation grants #2138259, #2138286, #2138307, #2137603, and #2138296.

Contributions

Z.Y. conceived the overall project and supervised the research. Z.Z. built the model architecture, performed the zeolites N_2 Adsorption simulations, and conducted the data analysis. S.B.K. and K.S. prepared the new MOF N_2/CO_2 separation dataset. Z.Z., Z.Y., and K.S. contributed to the development of model interpretability. All authors contributed to the preparation of the manuscript.

Competing interests

The authors declare no competing interests.